Received: 21 December 2021 | Revised: 30 May 2022 | Accepted: 20 July 2022 | Published on: 21 September 2022

DOI: 10.1002/qj.4352

Quarterly Journal of the Royal Meteorological Society RMetS

RESEARCH ARTICLE

On the effect of nocturnal radiation fog on the development of the daytime convective boundary layer: A large-eddy simulation study

Johannes Schwenkel[1] | **Björn Maronga**[1,2]

[1]Institute of Meteorology and Climatology, Leibniz University Hannover, Hannover, Germany

[2]Geophysical Institute, University of Bergen, Bergen, Norway

Correspondence
J. Schwenkel, Institute of Meteorology and Climatology, Leibniz University Hannover, Hannover, Germany.
Email: schwenkel@meteo.uni-hannover.de

Funding information
German Research Foundation, Grant/Award Number: MA 6383/1-2

Abstract

The potential effect of failing to predict nocturnal deep radiation fog on the development of the daytime convective boundary layer (CBL) is studied using large-eddy simulations. Typical spring and autumn conditions for the mid-latitudes are used to perform simulations in pairs. Fog formation is allowed in one simulation of each pair (nocturnal fog [NF]) and is suppressed in the other (clear sky [CS]). This allows for the identification of properties (temperature, humidity, boundary-layer depth), conditions, and processes in CBL development that are affected by fog. Mixing-layer temperatures and boundary-layer depths immediately after fog dissipation in CSs are shown to be up to 2.5 K warmer and 200 m higher, respectively, than the NF counterparts. Additionally, greater water vapor mixing ratios are found in the CSs. However, owing to greater temperatures, relative humidities at the CBL top are found to be less in CSs than in the corresponding NFs. This relative humidity difference might be an indication that cloud formation is suppressed to some extent. The magnitude of the differences between CSs and NFs during the day is mainly correlated to the fog depth (in terms of duration and liquid water path), whereas the key processes responsible for differences are the atmospheric long-wave cooling of the fog layer (for temperature development) and droplet deposition (for water vapor mixing ratio development).

KEYWORDS

boundary-layer development, diurnal cycle, large-eddy simulation, misrepresenting fog, PALM, radiation fog, turbulence

1 | MOTIVATION

Fog is a cloud in the vicinity of the Earth's surface characterized by a reduction of visibility to less than 1 km. Despite the rather small vertical extent, low wind speeds and negligible amount of precipitation compared with other clouds, fog still poses a threat to human life, especially in transportation (Haeffelin *et al.*, 2010). Fundamental and applied research have significantly improved fog forecasts and contributed to a broader and deeper understanding of

fog at the process level in the last decades. However, common numerical weather prediction (NWP) models still fail to predict a significant amount of fog events (Steeneveld *et al.*, 2015). Radiation fog is the most common continental fog type (e.g., Bergot, 2013). The misrepresentation of the life cycle of this type of fog (i.e., its onset, depth, and dissipation), as well as a lack of representation in NWP models, can be caused by several factors. A number of complex, small-scale processes (such as turbulent mixing, land–atmosphere interactions, aerosol and cloud microphysics, and radiation) that interact on different scales must be resolved or parametrized correctly (Steeneveld *et al.*, 2015). Likewise, the atmospheric conditions must be known precisely, because fog formation is sensitive to changes in temperature, humidity or soil moisture. An incorrect representation of subtle supersaturations could be generated from even small deviations in the forcing data and fog might fail to be predicted accurately (Rémy and Bergot, 2009). Capturing small-scale processes and precisely representing multilayered forcing data are hampered by the relatively large grid spacing commonly used in NWP.

Apart from the hazards associated with it, the presence of deep fog significantly alters the properties of the nocturnal boundary layer (NBL). The NBL is typically characterized by a stable stratification and weak forcings. These characteristics result in low or sometimes intermittent turbulence (Fernando and Weil, 2010). In contrast, convection can be triggered in the NBL by deep fog because the fog layer is optically thick to long-wave radiation; the atmosphere is destabilized from above because the net radiative loss occurs at the top of the fog (e.g., Nakanishi, 2000). Because of this energy loss, the sign of the turbulent sensible surface heat flux (SHF) is the opposite of what would typically be expected in the stable-stratified NBL and increased turbulence is produced. Therefore, differences between the stable NBL (SNBL) and foggy NBL might be caused by diabatic processes, such as modified long-wave cooling, short-wave absorption, turbulent mixing and entrainment, reduction of the total water content through droplet settling, and modified dewfall. Although the SNBL is quickly transformed into a convective boundary layer (CBL) after sunrise, the daytime convection might be influenced by the propagation of NBL properties into the day (Vilà-Guerau de Arellano, 2007).

In a previous study, van Stratum and Stevens (2015) found that the error resulting from misrepresenting the dry summertime SNBL (due to too coarse grid spacings) in large-eddy simulations (LESs) has a negligible influence on the daytime convection and bulk properties of the CBL. In a follow-up study by van Stratum and Stevens (2018), it was shown using a conceptual model that, even when humidity and radiation are accounted for, it is unlikely that fog or low clouds are formed during the night as a consequence of the overestimation of vertical mixing. The influence of non-resolved fog (assuming a maximum vertical extent of 50 m) for the summertime CBL development was also evaluated in their study as rather small. However, these studies were designed to discover if daytime convection is significantly influenced by the usage of low-resolution LESs, which the SNBL is not correctly resolved with. In addition to insufficient grid spacings, there are numerous other reasons for nocturnal fog to be misrepresented (e.g., inappropriate microphysical parametrization, errors in the initial conditions). Recently, it was shown in the model intercomparison of Boutle *et al.* (2022) that even sophisticated models revealed a large spread in simulating fog characteristics. Smith *et al.* (2018) demonstrated that, beyond model inefficiencies, subtle changes in humidity in the residual layer and wind-driven vertical mixing can have a significant impact on the development of radiation fog. Thus, this study is meant to complement the valuable results of van Stratum and Stevens (2018) by evaluating the physical effect of nocturnal fog on CBL development. Unlike van Stratum and Stevens (2015), the van Stratum and Stevens (2018) meteorological conditions for the transition months are applied because such conditions are more typical for nocturnal fog in the midlatitudes (Izett *et al.*, 2019). Spring and autumn conditions in the midlatitudes are associated with weaker incoming solar radiation to dissipate the fog layer after sunrise. An inadequate representation of such conditions is hence more likely to cause a stronger effect on CBL development.

In this article, the following questions will be answered:

1. What are the effects of nocturnal radiation fog on the development of the daytime CBL?
2. How long do these effects persist?
3. Which conditions and parameters amplify or reduce the influence of fog on CBL development?
4. What processes are responsible for differences observed?

To answer these questions, idealized LESs are performed in pairs (with and without fog formation possible). The diurnal cycle of a typical fog event observed at Cabauw (Netherlands) is modeled in the simulations. Radiative conditions between February and April are used. With the help of LESs, the diurnal cycle and the physical processes within the boundary layer (BL) can be modeled realistically and are less dependent on parametrizations compared to one-dimensional approaches.

Unfortunately, to examine the entire parameter space and obtain conclusions for all conceivable meteorological

situations prone to fog formation would be computationally uneconomical and, therefore, beyond the scope of this study. The objective of this work is rather to provide a quantitative estimate of the possible errors in simulating the daytime CBL properties induced by the absence of a deep fog event during night. Hence, our study is limited to one (but representative for typical local radiation fog) case setup, neglecting surface heterogeneities, trees, and orography. Moreover, we confine the cases investigated to situations with a deep nocturnal radiation fog that completely dissipates after sunrise. Thus, to investigate the influence of a fog layer that turns into a long-lasting stratus deck after dissipation is beyond the scope of this article.

The article is structured as follows: Background on the LES model and the setup of the numerical experiments used in this study are provided in Section 2. The results of the numerical experiments are presented in Section 3. Finally, a discussion and conclusion of this study is provided in Section 4.

2 | METHODOLOGY

2.1 | Model

In this study we use the PALM model system 6.0 (revision 4792) (Maronga *et al.*, 2020a). The model core is based on the incompressible Boussinesq-approximated Navier–Stokes equations, prognostic equations for potential temperature, and the total water mixing ratio. Discretization in space and time on the Cartesian grid is achieved by finite differences using a fifth-order advection scheme after Wicker and Skamarock (2002) and a third-order Runge–Kutta time-stepping scheme (Williamson, 1980), respectively. For the non-resolved eddies, a 1.5-order flux-gradient subgrid closure scheme after Deardorff (1980) is applied, which includes the solution of an additional prognostic equation for the subgrid-scale turbulence kinetic energy. The influence of different subgrid-scale models is discussed in Maronga and Li (2022).

Moreover, using embedded models considering land-surface interactions, radiative transfer, and cloud microphyscis, as well as the interactions among the model parts, PALM has the ability to cover the most important physical processes involved in fog development and the diurnal cycle. The land-surface model (LSM) consists of an energy balance solver for the skin temperature T_0 and a multilayer soil model, predicting the soil temperature and the soil moisture content. A rigorous description and evaluation of the PALM's LSM implementation are given by Gehrke *et al.* (2021). A coupling of the Rapid Radiation Transfer Model for Global Models (RRTMG) (Clough *et al.*, 2005) to PALM achieves the radiative transfer (in one-dimensional mode) for each vertical grid column. In particular, RRTMG calculates the radiative fluxes (short wave and long wave) for each grid volume while considering profiles of pressure, temperature, humidity, liquid water, and effective droplet radius. Three-dimensional radiation effects are neglected. Prognostic equations for the cloud droplet number concentration and cloud water mixing ratio as well as all cloud microphysical processes are described by using the embedded two-moment bulk cloud model based on parametrization formulated by Seifert and Beheng (2001; 2006. This scheme is extended by a parametrization for activation and a diagnostic treatment for diffusional growth based on the equations presented in Morrison *et al.* (2005).

In previous studies, PALM has been successfully applied to represent the stable BL (Beare *et al.*, 2006; Couvreux *et al.*, 2020; Maronga *et al.*, 2020b), radiation fog (Maronga and Bosveld, 2017; Schwenkel and Maronga, 2019; Boutle *et al.*, 2022), and diurnal cycles (Gehrke *et al.*, 2021).

2.2 | Numerical experiments

The design of the numerical experiments is based on the concept of running pairs of simulations, one allowing fog to form (in the following termed nocturnal fog [NF]) and the other where formation of liquid water is prohibited (in the following termed clear sky [CS]). Otherwise, identical initial conditions are applied. The initial conditions of the numerical experiments follow the idealized case used by Maronga and Bosveld (2017, fig. 4), which in turn is based on the observations of a deep radiation fog event from March 22–23, 2011, at the Cabauw Experimental Site for Atmospheric Research in the Netherlands. The initial profiles can be summarized as follows: Starting at $T_0 = 276$ K, a stable stratified BLr of 50 m with an initial temperature gradient of $\gamma_{bl} = 0.08\ \mathrm{K \cdot m^{-1}}$ is followed by a residual layer with $\gamma_{rl} = 0.01\ \mathrm{K \cdot m^{-1}}$. In this study, the model domain size is vertically extended (up to 1,230 m) in order to cover the vertical extent of the CBL developing during daytime. The value of γ_{rl} of the residual layer is used until the model top. Moreover, relative humidity (RH) decreases from 95% at the first grid level to 90% at 50 m and 85% at 400 m height. Subsequently, the water vapor mixing ratio decreases in such a way that RH reaches a value of 50% at 800 m and stays constant afterwards.

For all numerical experiments, cyclic conditions are used at the lateral boundaries, whereas at the model top the wind speed is fixed to the geostrophic value (varying for different parameter runs). In addition, a sponge layer is applied starting at a height of 1,000 m in order to prevent

gravity waves from being reflected at the top boundary of the model. The simulation start time is varied from around 2100 UTC to 0300 UTC but with a fixed end at 1600 UTC. The LSM is initialized with a short grassland canopy and an eight-layer soil configuration as suggested by Gehrke *et al.* (2021). The bulk cloud model, which also includes a scheme for activation, is initialized with a background aerosol concentration of 100 cm^{-3} composed of ammonium sulfate. Note that in real, continental environments, aerosol concentrations are typically higher. However, as our dry aerosol radius is relatively large, this aerosol concentration does illustrate the relevant fraction of aerosol, which can act as cloud condensation nuclei. As a result, an average droplet concentration of approximately 80 cm^{-3} (varying in space and time) is found in our simulations. We consider droplet deposition by sedimentation, assuming that droplets are distributed log-normally and falling in a Stokes regime (Ackerman *et al.*, 2009). Aerosol scavenging due to droplet deposition is not included; this effect is discussed, for example, in Schwenkel and Maronga (2020). Also, we do not consider turbulent droplet deposition by vegetation, which was modeled, for example, by Mazoyer *et al.* (2017). Further global parameters for simulation steering can be found in Table 1.

The difficulty of representing the diurnal cycle accurately is, on the one hand, to have sufficiently small grid spacings to simulate the weak turbulence and relatively small eddies at night. On the other hand, the model domain must be large enough to capture the largest eddies during the day (Brown *et al.*, 2002). Given limited computational resources, this combination is always a trade-off between precision and costs. In this study, a novel but simple approach is used, which can briefly be phrased as "cyclic-restart," a mixture between the cyclic-fill method after restarting of the simulation. This method implies that the simulation is stopped once the BL has reached a height of 350 m for the first time, which corresponds to 2.5 times the horizontal model domain size and provides a proxy for the minimum horizontal extension needed to resolve the largest turbulent eddies. The threshold of 350 m is reached in the simulations between 0930 UTC and 1230 UTC, depending on the specific parameter case. Thereafter, the model domain is extended horizontally by a factor of 2.5. For this procedure, the so-called cyclic-fill method is used; that is, the added areas are filled cyclically with the state of the atmosphere at the end of where the precursor run has stopped (Figure 1). This procedure requires non-integer factors for the domain extension, as otherwise all turbulent structures are numerically identical and will develop undisturbed up to the last decimal place equally. In addition, the cloud model is also switched on for the CSs during restart, so that the formation of BL clouds during daytime is not suppressed. However, none of the experiments conducted is found to feature the development of daytime clouds.

Based on sensitivity studies (Section 3.1), an isotropic grid spacing of $\Delta = 3$ m is used; similar grid spacings for simulating the SBL or fog are used, for example, by Beare *et al.* (2006) and Wærsted *et al.* (2019). As outlined before,

TABLE 1 Model parameters and initial conditions of the numerical experiments for all large-eddy simulations (unless otherwise explicitly stated)

Description	Symbol	Value
Grid spacing (m)	Δ	3.0
Vertical model extent (m)	H	1,230
Horizontal model extent (m)		
Nighttime	$L_{x,y}$	810
Daytime	$L_{x,y}$	2,025
Surface pressure (hPa)	p_0	1,040
Skin temperature (K)	θ_0	276.0
Roughness length (cm)	z_0	5
Surface humidity ($g \cdot kg^{-1}$)	q_0	5.5
Time-step radiation (s)	Δt_{rad}	60.0
Short-wave albedo	α	0.14
Aerosol concentration (cm^{-3})	N_a	100.0
Mean aerosol radius (μm)	r_a	0.012
Geometric standard deviation of aerosol distribution	σ_a	1.8
Skin-layer conductivity ($W \cdot m^{-2} \cdot K^{-1}$)	Λ	4.0
Soil moisture ($m^3 \cdot m^{-3}$)	m_k	0.4
Saturation moisture ($m^3 \cdot m^{-3}$)	m_{sat}	0.6

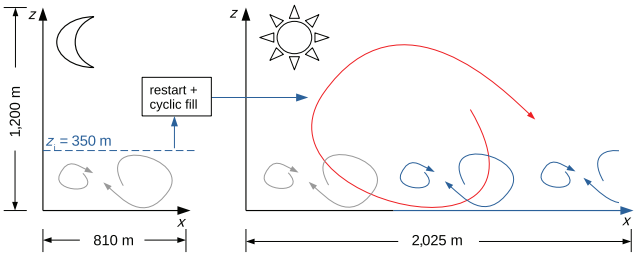

FIGURE 1 Domain layout and termination criterion of night- and daytime simulation [Colour figure can be viewed at wileyonlinelibrary.com]

TABLE 2 Overview of simulation pairs conducted

Simulation-pair name	$R_{sw,max}$ ($W \cdot m^{-2}$)	Day of the year	Simulation start time (UTC)	Geostrophic wind ($m \cdot s^{-1}$)
Parameter simulations				
R700S21U5.5	700	March 23	2100	5.5
R700S21U2.8	700	March 23	2100	2.75
R700S21U1.4	700	March 23	2100	1.375
R700S23U5.5	700	March 23	2300	5.5
R700S01U5.5	700	March 23	0100	5.5
R700S03U5.5	700	March 23	0300	5.5
R500S21U5.5	500	February 21	2100	5.5
R600S21U5.5	600	March 7	2100	5.5
R800S21U5.5	800	April 7	2100	5.5
R900S21U5.5	900	April 21	2100	5.5
Additional simulations for process analysis				
R600S21U2.8	600	February 21	2100	2.75
R800S21U2.8	800	April 7	2100	2.75
R600S23U2.8	600	February 21	2300	2.75
R800S23U2.8	800	April 7	2300	2.75
R800S23U5.5A200	800	April 21	2300	5.5
R600S21U5.5A50	600	February 21	2100	5.5
R600S21U5.5A25	600	March 7	2100	5.5

Note: The baseline simulation pair is indicated in bold.

we work with two different model domains in each simulation. The nighttime domain has $270 \times 270 \times 225$ grid points in x-, y-, and z-directions, respectively, while the daytime domain is running on $675 \times 675 \times 225$ grid points. Accordingly, the nighttime domain is 810 m × 810 m and the daytime domain covers 2,025 m × 2,025 m horizontally. The vertical model extent is the same for both layouts and ends at 1,230 m (by applying grid stretching above 500.0 m, but limiting the vertical grid spacing to a maximum of 15 m).

In the parameter simulations we vary the geostrophic wind speed in order to represent different strengths or turbulent mixing. Furthermore, we vary the day of the year to account for different solar radiation forcing (both intensity and length of the day). Finally, we are also implicitly varying the fog thickness by prescribing different simulation start times (but all being after sunset). Thus, the fog has more time to develop vertically during nighttime until sunrise. The range of parameters represents a broad spectrum of possible meteorological conditions in which nocturnal radiation fog is likely to form. However, cases in which the fog does not completely dissipate and turns into a low-level stratus cloud are excluded in order to be able to link the appearing differences between CS and NF unambiguously to the presence of fog during nighttime. All parameter simulation pairs conducted are listed in Table 2. The nomenclature of the simulation pairs is as follows: First, the maximum incoming solar radiation at noon (e.g., R700 is equal to approximately 700 $W \cdot m^{-2}$) is given. Second, the starting point of the simulation is declared (e.g., S21 means a model start at solar noon 2100 UTC). Third, the geostrophic wind conditions are stated (e.g., U5.5 implies a geostrophic wind speed of 5.5 $m \cdot s^{-1}$). For the purpose of analyzing processes that are responsible for differences between CS and NF, we added seven further simulation pairs (see Table 2), consisting of cross-combinations of the previous cases; for example, lower wind speeds and with a different day of the year, and different background aerosol conditions from 25 to 200 cm^{-3} (indicated with capital A). In the following, δ is used to denote the difference of a quantity between the CS and NF cases, wherea Δ is the grid spacing. Since case R700S21U5.5 is closest to the conditions of the Cabauw observations, we define it as the baseline simulation pair.

2.3 | Analysis of process contributions of temperature and humidity budget

This section describes how we separate the modeled temperature and humidity tendencies into contributions from different physical processes. By doing so, we are able to evaluate processes responsible for differences between CS and NF caused by the presence of fog. The general approach is similar to the method applied by Wærsted *et al.* (2019) assessing processes leading to fog dissipation. In general, assuming horizontal homogeneity and neglecting non-local processes, the temperature within the atmosphere within the analysis height H_a is changed by the SHF, long- and short-wave radiation divergence ($R_{lw} + R_{sw}$), and by microphysics (F_{micro}); that is, the release of latent heat due to condensation or evaporation. In this study we choose $H_a = 1{,}000$ m, which is the model domain up to the sponge and larger than the maximum modeled BL heights (BLHs) of all simulations. Choosing H_a larger than the BLHs of all parameter simulations implicitly eliminates the contribution by mixing with the free atmosphere for changes in temperature and water vapor mixing ratio. Thus, the temperature budget within H_a (in the following, differences averaged over H_a are denoted with angle brackets) can be written as

$$\left\langle \frac{d\theta}{dt} \right\rangle = \mathrm{SHF} + R_{lw} + R_{sw} + F_{micro}. \quad (1)$$

Analogously, the water vapor mixing ratio within H_a is altered by the turbulent latent surface heat flux (LHF), which can be split into a contribution by the evapotranspiration of the vegetation (LHF_{veg}) and by the condensation or evaporation of dew (LHF_{liq}). F_{micro} includes condensation (evaporation) of water vapor to liquid (of liquid to water vapor) and contributes as a loss (gain) for the water vapor budget. The water vapor mixing ratio budget for the modeled atmosphere is

$$\left\langle \frac{dq}{dt} \right\rangle = \mathrm{LHF}_{veg} + \mathrm{LHF}_{liq} + F_{micro}. \quad (2)$$

For a time-integrated analysis of process contributions we integrate up to the point in time where the temperature and humidity difference within H_a after fog dissipation (i.e., within the analysis period) differs the most between CS and NF (hereafter denoted by $t_{a,\theta}$ and $t_{a,q}$, respectively). In this regard, F_{micro} can be substituted by the deposition of fog droplets (F_{dep}) assuming that all condensed water that has not been deposited to the surface has been evaporated again after fog dissipation. How the right-hand side terms of Equations 1 and 2 are derived from the model output is documented in the Appendix.

3 | RESULTS

3.1 | Sensitivity study

We first present the results of a grid sensitivity study of the baseline simulation. Based on these results, the grid spacings for the parameter studies are selected. For this purpose, we perform simulations with isotropic grid spacings of $\Delta = 1.5$, 3.0, 6.0, 12.0, 24.0 m. As outlined earlier, the NBL is known to be especially sensitive to the numerical grid resolution due to possibly underresolved turbulence. Figure 2 shows profiles for the horizontal wind velocity, potential temperature, and liquid water mixing ratio of the sensitivity simulations 2 hr before sunrise (upper row) and at noon (1200 UTC, lower row). The most obvious differences can be observed during night in both wind speed and potential temperature, with pronounced differences between a foggy convective NBL and an SNBL. Additionally, large differences are found among the cases using different grid spacings, especially for the CSs at night (Figure 2a,b). Those differences are caused by an overestimation in vertical mixing when using too coarse grid spacings, leading to underestimation of the near-ground temperature gradient (Figure 2b; see (van Stratum and Stevens, 2015)). Even though the differences are smaller for the NFs, since the NBL is convectively evoked by the deep fog we observe up to 40% lower liquid water mixing ratios for larger grid spacings. However, the profiles of q_l between cases with $\Delta = 1.5$ m and $\Delta = 3.0$ m match quite well; thus, we conclude that the fog is sufficiently resolved with $\Delta = 3.0$ m.

At noon (1200 UTC), where both NFs and CSs are convective, simulation results are less sensitive to the chosen grid spacing. Especially for the CSs, the temperature profiles are quite similar and do not show the deviation observed during the night (Figure 2), which is in line with the findings of van Stratum and Stevens (2015). However, for the NFs we observe deviations up to 0.5 K for θ in the BL. As we want to investigate the influence of a foggy NBL on daytime convection as precisely as possible, such errors as found for grid spacing larger than $\Delta = 3.0$ m in the representation of fog are not negligible. Based on these sensitivity studies, we used a grid spacing of 3.0 m for the parameter studies.

3.2 | Diurnal cycle

To identify processes that cause NF affecting the CBL development and to determine which meteorological conditions intensify or mitigate this impact, we employ a set of parameter simulations in which we vary the radiation conditions, the wind speed, and the fog depth (see Table 2).

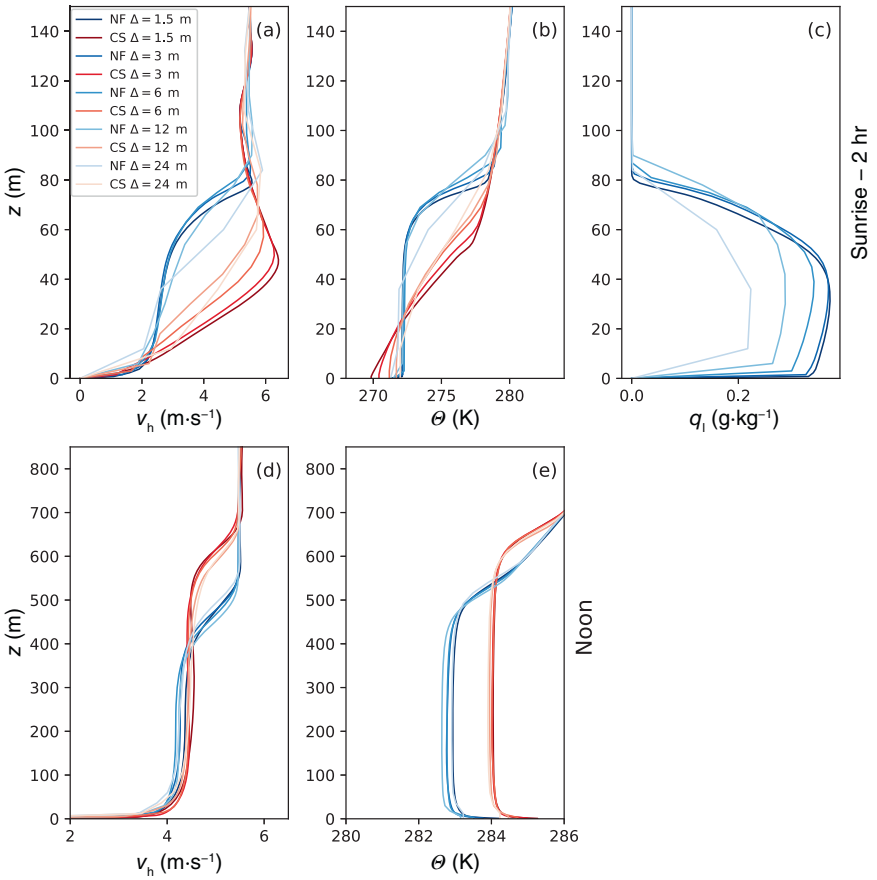

FIGURE 2 Profiles (horizontally averaged) of the horizontal wind velocity, (a,c) potential temperature (b,d) liquid water mixing ratio (e) for different grid spacings of the baseline simulations 2 hr before sunrise (upper row) and at noon (lower row) [Colour figure can be viewed at wileyonlinelibrary.com]

We conduct simulations for five different days of the year between February and end of April, three different wind speeds (u_g = 5.5, 2.75, and 1.375 m·s^{-1}), and four different fog depths implicitly achieved by using various simulation starting points (2100, 2300, 0100, and 0300 ,UTC); that is, by varying the length of the night where short-wave radiation is absent.

We simulate the diurnal cycle (starting at night until 1600 UTC of the next day) for different parameter study pairs. The general BL development during the diurnal cycle, which differs for the individual parameter cases, is outlined exemplarily for the baseline simulation in Figure 3 in terms of the vertical velocity shown as instantaneous cross-section for three different stages (top row: at night 0500 UTC, during fog; center row: shortly after dissipation around 1100 UTC; and bottom row: in a fully developed CBL at 1400 UTC) during the diurnal cycle. At night, a well-mixed fog layer (marked by contour lines) with a height of 80 m in the NF (left column) has developed, whereas the CS (right column) exhibits a somewhat lower BLH and lower vertical wind speeds (shear driven) due to a stable stratification. After sunrise, the fog completely dissipates (at 1100 UTC) and the mixing layer reaches a BLH of 290 m, whereas the BLH in the CS is as high as 480 m. At 1400 UTC, both BLs are cloud free and convective. The CS, however, exhibits a 150 m deeper BL.

Figure 4 shows time series for simulation pairs in which the day of the year, and hence incoming solar radiation conditions, is varied. The LWP (Figure 4a) of the fog layers increases equally in all simulations as long as sunlight is absent. Beginning with sunrise in the R900S21U5.5, the LWP growth rate decreases and subsequently the LWP starts to decrease. By time the fog (the green shaded areas show the time where fog exists by definition; i.e., visibility is less than 1,000 m at 2 m height) lifts and remains as a low-level cloud for 1–3 hr until the liquid water has been completely dissipated. The presence of fog and low-level clouds significantly alters the near-surface radiation balance (Figure 4b). On the one hand, at night, the surface radiation balance is less negative in the NFs compared with the CSs; that is, surface cooling rates are stronger in cases without fog as the fog layer intensifies long-wave counter-radiation. On the other hand, after sunrise, the effect of an increased atmospheric albedo (i.e., the relatively light fog layer) outweighs the increased atmospheric long-wave radiation for the NF, resulting in higher net surface radiation values for the CS.

The focus in this study will be on the differences within the period after all liquid water is dissipated in the NFs and the surface short-wave radiation balance is the same for NFs and CSs (defined by $|\delta R_{sw,in}| < 2\,W{\cdot}m^{-2}$). Using a threshold of $|\delta R_{sw,in}| = 0\,W{\cdot}m^{-2}$ is not feasible, as different

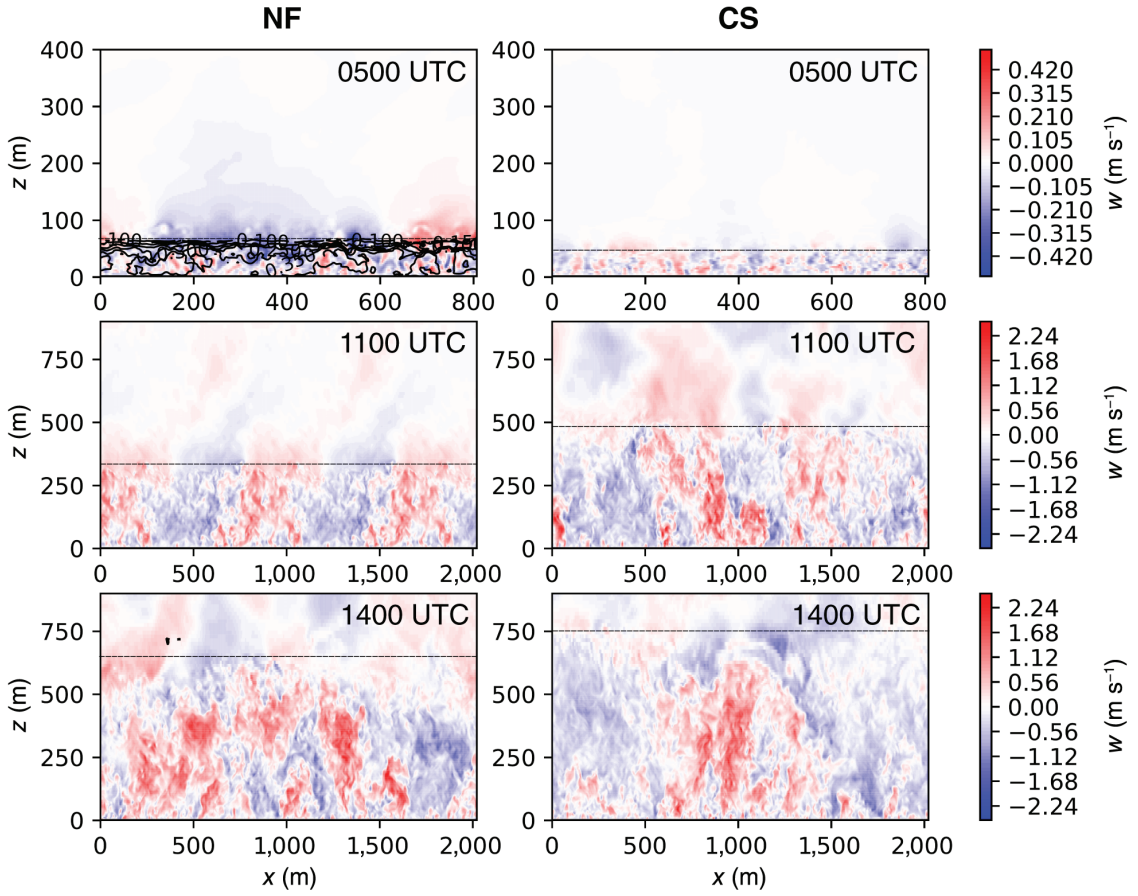

FIGURE 3 Instantaneous x–z sections for vertical velocities at $y = 0$ m for nocturnal fog (NF, left column) and clear sky (CS, right column) at 0500 UTC (top row), 1100 UTC (center row), and 1400 UTC (bottom row) for the baseline simulation. The black dashed lines indicate the domain-averaged boudary-layer height. Contour lines for the foggy case at 0500 UTC show the liquid water mixing ratio [Colour figure can be viewed at wileyonlinelibrary.com]

temperature and humidity profiles cause slight deviations in the incoming solar radiation between NFs and CSs. The length of the analysis period is shaded in Figure 4c,d. Shown are the differences of the 2 m potential temperature (c) and BLH (d) between the NFs and CSs.

Although the radiative forcing (sunrise, zenith, and thus strength of incoming solar radiation), is considerably modified within the parameter cases, we observe the same qualitative temperature trend for all simulations (Figure 4c). At 2300 UTC the fog has formed in the NFs within the first grid level and about 0.8 K higher temperatures appear for the CSs near the ground. As long as the fog top is shallow, the radiative cooling rate (3–4 K·hr^{-1}) of the fog cools the near-surface layers. However, during the night, after fog has become optically thick and deeper, which suppresses net surface cooling and amplifies vertical mixing, higher near-surface temperatures in the NFs are observed (up to 2 K). Indeed, as long as the CSs are stably stratified this tendency in the temperature deviation is only present for the near-surface regions. An analysis for the temperature within H_a exhibits also higher temperatures for the CSs during the night, as the vertically integrated cooling is stronger for the NFs (see next section). Maximum differences between CSs and NFs in the 2-m temperature can be found shortly after sunrise, showing a deviation up to 4.5 K. Afterwards, at the beginning of the analysis period, differences between 2.5 and 2.0 K are simulated, which decrease (exponentially) down to deviations between 0.5 and 2.0 K at 1600 UTC. The decline of the differences can be explained by approximately 25% larger values of the Bowen ratio (B = SHF/LHF) in the NFs; that is, in the NFs; more energy is transferred into sensible heat, whereas in the CSs more energy is transferred into latent heat after fog dissipation (will be shown later).

Furthermore, in all simulation pairs, the BLH is higher for CSs than with the NFs within the analysis period. The deviations are in the range of 150.0–200.0 m at the beginning of the analysis period and, in contrast to the exponential temperature declination, tend to decrease linearly (discussed later) in time, yielding deviations between 200 m and 100 m at 1600 UTC. However, for

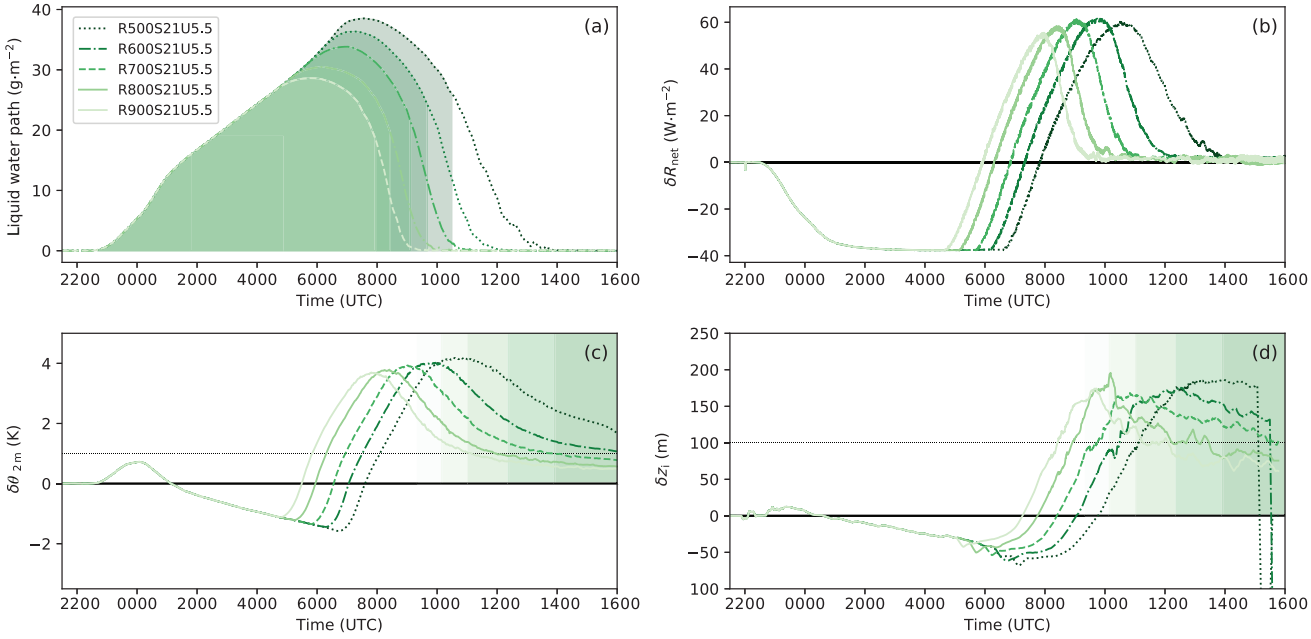

FIGURE 4 Time series for parameter studies R500S21U5.5–R900S21U5.5 showing the liquid water path of the fog for (a) the nocturnal fog (NF) case and the deviations (clear sky [CS] minus NF) of the (b) surface radiation balance, (c) potential temperature at 2 m, and (d) boundary-layer height (BLH). The BLH is calculated as an average over 10 min. Shaded areas in (a) indicate the period of fog (by definition of visibility at 2 m height). Shaded areas in (c) and (d) mark the analysis period, with the same radiative forcing between CS and NF [Colour figure can be viewed at wileyonlinelibrary.com]

R500S21U5.5 (corresponding to end of February), no decrease in BLH is observed, which can be explained by the low incoming solar radiation at the time of fog dissipation insufficient to compensate the deviations. The collapse of the BLH deviations for the simulations R500S21U5.5 and R600S21U5.5 marks the decay of daytime convection due to a negative surface net radiation. As a result, we observe that the absolute differences in temperature and BLH increase with decreasing incoming solar radiation. But it must be mentioned that the available solar incoming radiation, being the major forcing for the SHF and known to be the prime process for fog dissipation (Wærsted *et al.*, 2019), is thus also correlated to the fog depth and life time.

Within the parameter runs (based on the radiation conditions for mid-March) for lower turbulent mixing (Figure 5) as well as different fog depths (implicitly induced by later simulation starts; Figure 6), we also observe higher 2-m temperatures as well as larger BLH for all parameter runs within the analysis period for the CS compared to the NF. Both cases with lower turbulent mixing (achieved by prescribing lower geostrophic wind speeds) reveal an earlier fog formation (about 30 min). Decreased turbulent mixing enhances surface cooling and, as a result, air becomes supersaturated earlier, which was also simulated in, for example, Bergot and Guedalia (1994) and Steeneveld and de Bode (2018). Once fog has formed, higher turbulent mixing accelerates the vertical propagation by stronger entrainment and a subsequent cooling of entrained air masses down to saturation. Figure 5a shows that lower turbulent mixing cases lead to lower LWPs, as the vertical development is retarded. Despite the higher LWP for the baseline simulation, a higher temperature within the BL and stronger mixing favor an earlier fog dissipation for this case (30 min to 1 hr earlier with respect to R700S21U2.8 and R700S21U1.4). Indeed, the effect of turbulent mixing on the life cycle of fog is controversially discussed in the literature (Bergot and Guedalia, 1994). In contrast to our findings, Smith *et al.* (2018) reported that stronger turbulent mixing weakens fog development during the night. Conclusively, turbulent mixing can facilitate or impede fog development and dissipation, which strongly depends on the thermodynamic profile of the overlying air (whether mixed air is close to saturation or relatively dry and warm) (Wainwright and Richter, 2021). It is noteworthy that simulation pairs with a geostrophic wind of 2.75 and 1.375 $m \cdot s^{-1}$ show only very small differences between each other in terms of LWP. This non-linear behavior indicates that the NF cases with lower turbulent mixing experience a transition in the turbulence regime as soon as deep fog has formed. From this point on, vertical mixing triggered by cloud-top cooling prevails over vertical mixing caused by wind shear. Although the fog development behaves similarly, decreased turbulent mixing leads to increased nocturnal 2-m temperature deviations between NFs and CSs. Though the NF cases for both decreased mixing cases

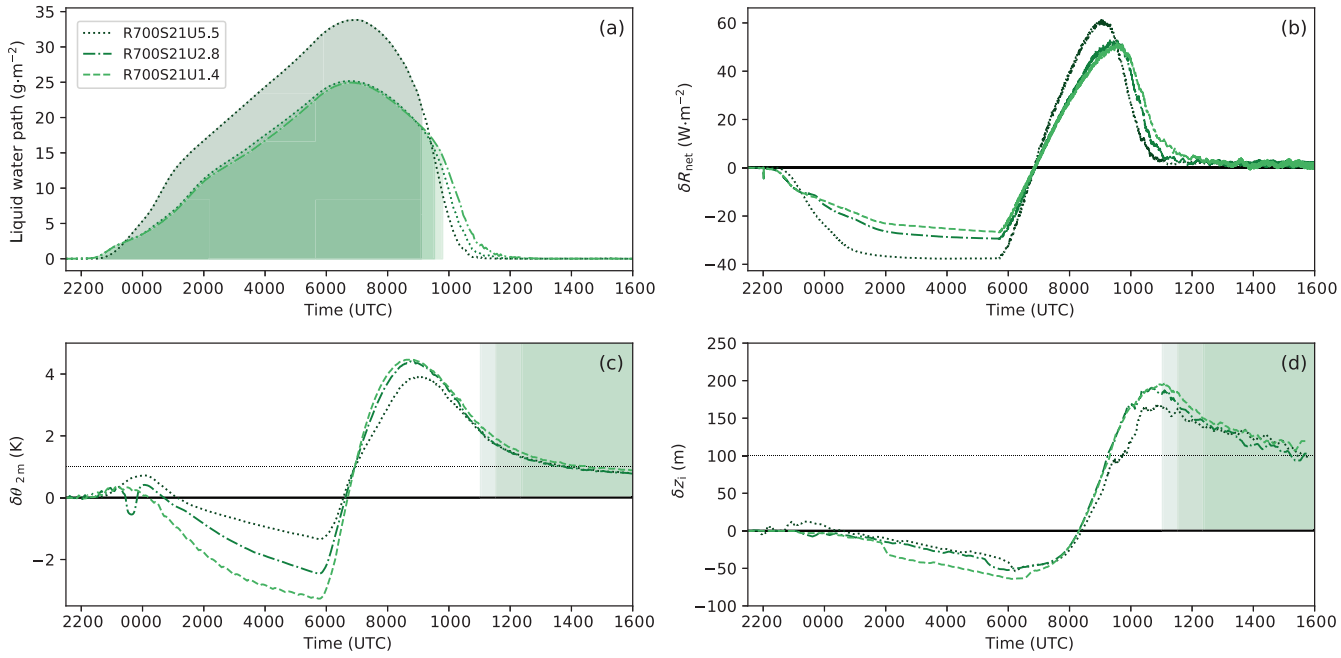

FIGURE 5 Same as Figure 4, but for parameter studies R700S21U1.4–R700S21U5.5 [Colour figure can be viewed at wileyonlinelibrary.com]

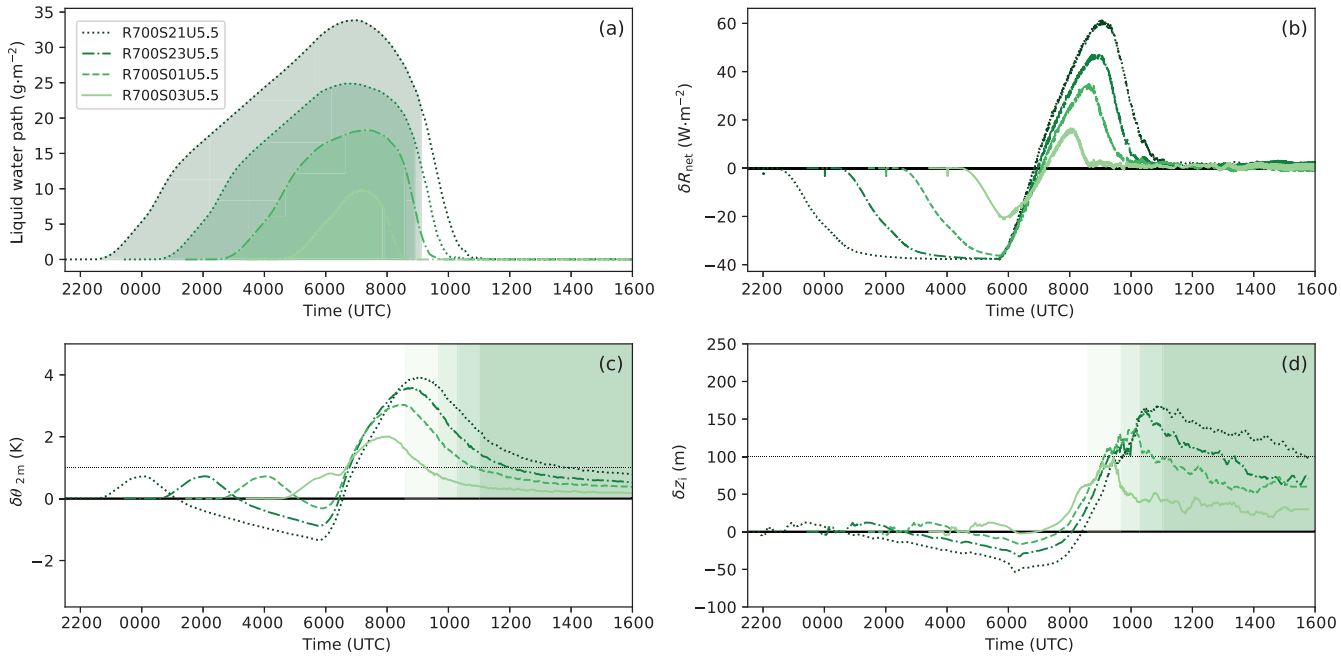

FIGURE 6 Same as Figure 4, but for parameter studies R700S21U5.5–R700S03U5.5 [Colour figure can be viewed at wileyonlinelibrary.com]

show a very similar BL structure, those differences are caused by the enhanced cooling of near-surface air due to a decreased vertical heat transport for R700S21U1.4. Nevertheless, within the analysis period, all simulations, regardless of the strength of turbulent mixing, reveal nearly identical deviations for the 2-m temperature and BLH. This is explained by the fact that a larger LWP (after sunrise) causes stronger differences in the radiation balance (see Section 3.3), which counteracts an earlier dissipation due to stronger vertical mixing.

Furthermore, the simulations with different fog depths show distinctly different LWPs and also fog heights (not shown). The later the simulation starts, the less time the fog layer has until sunrise and, therefore, the less time to

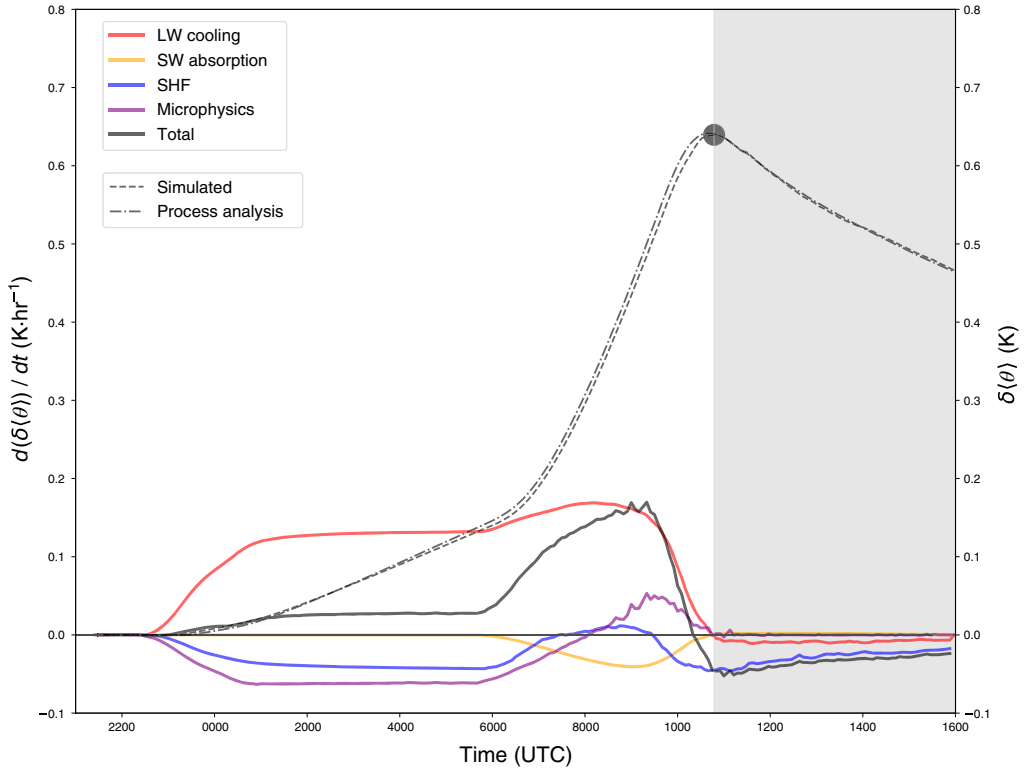

FIGURE 7 Time series for the differences of clear sky (CS) minus nocturnal fog (NF) in process-level contributions on temperature integrated over height H_a for the baseline simulation. The black solid line shows the total heating rate of CS minus NF, and the other lines represent the process contributions outlined in Equation (1). The right *y*-axis shows the simulated temperature difference within H_a, and the temperature difference by the process analysis is shown. The black marker shows the point in time where the maximum temperature difference after fog dissipation occurs. The gray shaded area marks the time span without fog. LW, long wave; SHF, sensible surface heat flux; SW, short wave [Colour figure can be viewed at wileyonlinelibrary.com]

develop before the BL warms up. Accordingly, the simulation (NF case) that starts at 0300 UTC has a maximum LWP of 10 g·m^{-2} and maximum fog height of 92 m, whereas for the simulation lasting the longest the LWP is three times higher with twice the fog height. Additionally, different simulation starting times also shorten the period in which surface cooling of the BL occurs (by a shorter nocturnal phase) and thus lead to higher BL temperatures with later simulation starts. Again, as in the parameter studies for different days of the year, higher LWPs lead to a later dissipation after sunrise—for example, as also found by Toledo *et al.* (2021)—of the fog layer and correlate with stronger differences between the NF and CS in temperature and BLH. Likewise, for the cases where the fog lasts the shortest and remains relatively thin, rather small differences from the comparison of CSs and NFs can be seen, but these nevertheless persist until the end of the analysis period. In summary, we can conclude that all NFs generally tend to lower BL temperatures as well as lower BLHs than the CSs do within the analysis period.

3.3 | Process-level analysis

Up to this point, we analyzed the parameter simulations pairs individually while changing only one of the parameters day of the year, starting point and geostrophic wind speed at a time. Indeed, the change of a single parameter (e.g., the day of the year) alters several interacting processes, for example, the absolute incoming solar radiation, the time of sunrise and consequently the depth of fog layer as well as the fog dissipation time. Therefore, we address this section to analyze which processes are the most important for the potential of fog to alter CBL development during daytime. Besides, we want to identify key parameters which crucially control the strength of the fog impact.

3.3.1 | Process-level analysis on temperature

Following the approach presented in Section 2.3, Figure 7 shows time series for differences in heating/cooling rates

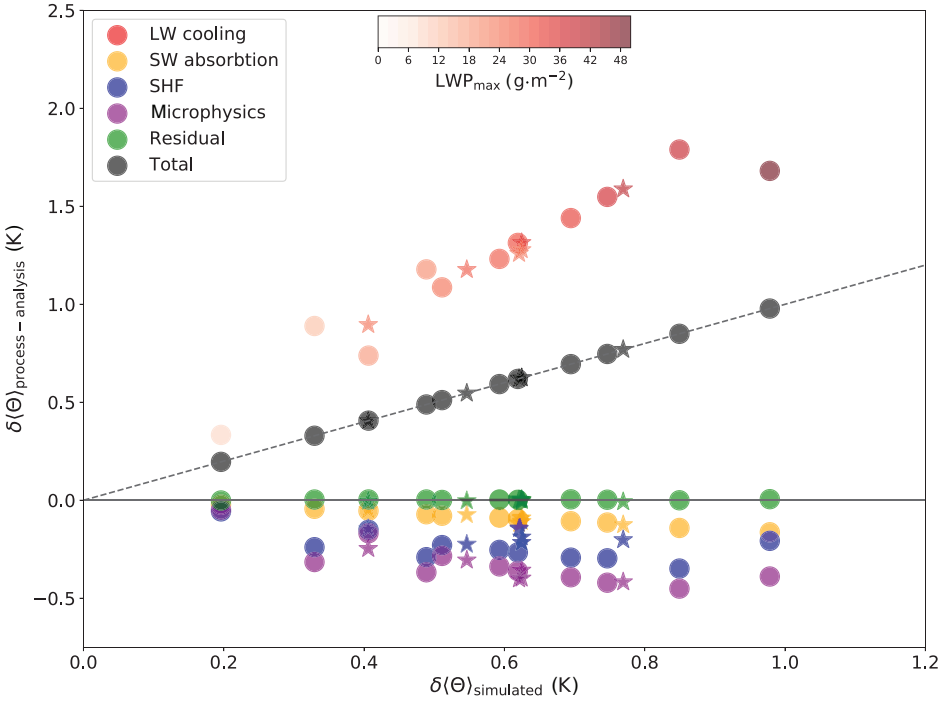

FIGURE 8
Integrated-in-time temperature differences within the air volume from the surface to contributions by atmospheric long-wave (LW) cooling, atmospheric short-wave (SW) absorption, surface sensible heat flux (SHF), latent heat, and residual versus maximum bulk temperature difference. Each dot represents the difference within a simulation pair at $t_{a,\theta}$. The sum of all contributions is shown by the black marker. The different opacity for LW cooling markers indicate the maximum liquid water path (LWP) of the fog layer. Simulations with lower wind speeds are marked by asterisks [Colour figure can be viewed at wileyonlinelibrary.com]

for the baseline simulation pair. The simulated and expected (by the contributions of the process analysis) temperature differences are illustrated with the black dashed and dotted lines on the right axis. Moreover, the time-integrated process analysis for all simulation pairs is shown in Figure 8.

The temperature difference between CS and NF increases in time until the fog is dissipated (Figure 7). Initially, the absolute heating rate is relatively constant at 0.025 K·hr^{-1}. After sunrise, however, the slope increases sharply as effective cooling occurs in the case of NF as a consequence of the evaporation of the fog layer. At the maximum we found a 0.62 K higher temperature for CS compared with NF. Note that the temperature difference within the BL might be up to two times (or more) the value as the BLH is about the half (or even less) of H_a at that time. After fog dissipation, the temperature difference within H_a is decreasing linearly associated with negative total cooling (quasi-constant) rates for CS minus NF. The quasi-constant difference in the heating-rate can also explain the linear decrease in BLHs (Figures 4–6). Growth of the BL is mainly caused by encroachment. Consequently, a constant difference in the heating-rate difference (between CS and NF) causes a linear decrease in BLH difference. Comparing the simulated temperature trend with the contributions achieved by Equation (1), we see that the temperature budget closes well during the diurnal cycle. This rather small differences might be caused by the approximation assumptions made for Equation (A1). Starting from fog formation until fog dissipation, radiative cooling reveals the largest net warming rates (≈0.13 K·hr^{-1}) between CS and NF. As, after fog formation, the CS has higher water vapor mixing ratios (leading to a stronger long-wave emission), radiative cooling is higher than for NF during daytime.

This behavior is also found for all the other parameter runs; that is, the difference in long-wave cooling leads to most of the BL temperature differences between the NFs and CSs (Figure 8). At maximum this is by +1.75 K, reflecting the strong emission of long-wave radiation at the fog top in the NFs, which cools the BL. While for CS conditions the atmospheric long-wave cooling is comparatively small (in our case about 0.6 K·hr^{-1}), cooling rates increase rapidly in the presence of fog (up to 6.0 K·hr^{-1}). As clouds are almost a black body within the infrared spectrum, the strength of radiative cooling correlates to the optical depth, which in turn depends on the cloud depth, the water content, and droplet size distribution (Mellado, 2017). Thus, unsurprisingly, we observe a correlation (to some extent) of the strength of radiative cooling to the maximum LWP. However, besides the strength of cooling rates, the temperature change by long-wave cooling depends on the lifetime of the fog (which is, inter alia, linked to the depth of the fog but might also be affected by turbulent mixing). The contribution by microphysics is mitigating the warming effect of long-wave cooling as for NF. As long as water vapor is condensing, the release of latent heat increases the temperature in NF (resulting in a negative contribution for CS minus NF). During fog dissipation, however, this leads to a temperature decrease in NF as water is evaporating. Integrated over time, microphysics is the largest contributor for warming the NFs, which is up to −0.45 K

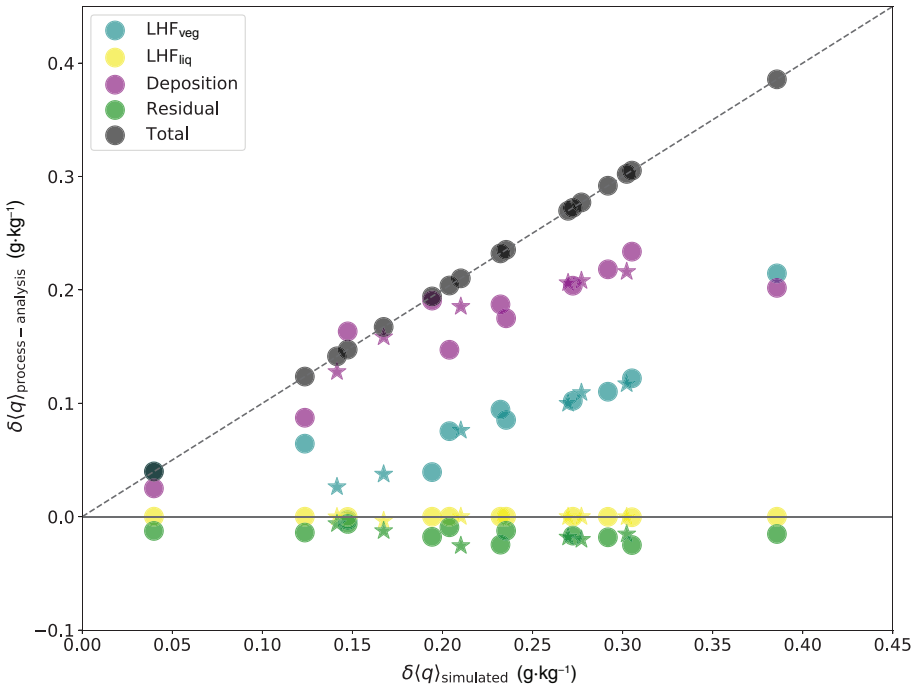

FIGURE 9 Integrated-in-time humidity difference within the air volume from the surface to HA contributions by evapotranspiration of plants, dewfall, droplet deposition, and the residual source versus maximum bulk humidity difference. Each dot represents the difference within a simulation pair at $t_{a,q}$. The sum of all contributions is shown by the black marker. Simulations with lower wind speeds are marked by asterisks [Colour figure can be viewed at wileyonlinelibrary.com]

(Figure 8). If all condensed liquid were to completely evaporate during the fog life cycle, this contribution would be net zero. Deposition of fog droplets, though, constantly removes liquid from the atmosphere and consequently evokes an imbalance between latent heat by condensation and evaporation the NFs experience a net warming. Moreover, the SHF contributes for all simulation pairs to a larger energy input (equivalent to negative difference) in the NFs (Figure 8). This is mainly explained by the stronger surface cooling during night for the CSs (Figure 7), as the surface net radiation gets more negative (and in turn leads to a stronger negative SHF) for the CSs (due to less reflected long-wave radiation, as no cloud is present) than in the NFs. After sunrise, there is a short period in time where the SHF is larger in the CSs caused by a stronger heated surface, though this is mitigated by the reflection of the fog layer in the NFs (Figure 7). This contribution is one order of magnitude lower than the stronger surface cooling at night, as the period where the SHF in the CS is stronger than in the NF is very short (90 min) and the amplitude in the difference is smaller. Subsequently, the SHF difference becomes negative again (i.e., indicating that the NF cases are more strongly heated by the surface), which leads to a decrease in the temperature deviation between CS and NF (Figure 7). This is explained by larger values of the Bowen ratio for the NFs after fog dissipation; that is, more energy is transferred to sensible heat than to latent heat, resulting in a stronger temperature increase (and thus explaining the reduction in the difference between CS minus NF within the analysis period). Nonetheless, the contribution of the SHF shows relatively similar values in the range of −0.15 to −0.4 K (Figure 8). After sunrise, heating due to atmospheric short-wave absorption also contributes to the temperature changes, which is larger for the NFs. Though the CS atmosphere is relatively transparent for short-wave radiation, the foggy atmosphere absorbs more short-wave radiation and leads to an increase in temperature. After fog dissipation, both NF and CS are cloud free and differences in heating rates due to short-wave absorption have vanished (Figure 7). Integrated-in-time differences between NFs can be quantified as −0.05 up to −0.2 K (Figure 8). Indeed, differences induced by short-wave heating are relatively small compared with contributions by long-wave cooling, microphysics, and SHF. Moreover, for all cases, a residual very close to zero is observed (Figure 9). This indicates that the process-level analysis covers the most relevant processes. To conclude, the temperature differences in the atmosphere between CS and NF have their origin in the night. The largest contribution to the temperature difference is cloud-top cooling, which in our case is a more powerful cooling process for the atmosphere than the nocturnal cooling from the surface. After fog dissipation, the temperature differences decrease due to the higher Bowen ratio for NF compared with CS.

3.3.2 | Process-level analysis on water vapor mixing ratio

Besides the temperature and BLH, the misrepresentation of fog also affects the water vapor content and the RH of the daytime CBL, and hence cloud formation during daytime.

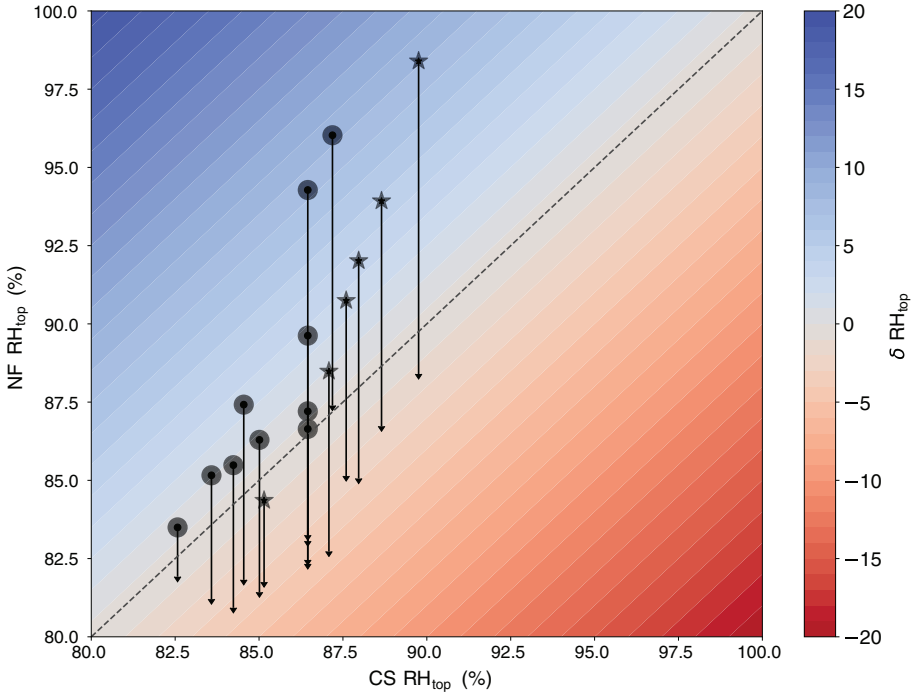

FIGURE 10 Boundary-layer (BL) to prelative humidity (RH) of nocturnal fog (NF) versus BL top RH of clear shy (CS) at noon (1200 UTC). The background illustrate the strength of the deviation between CS and NF, and the arrows indicate the RH drop by higher BL temperatures for the CS cases [Colour figure can be viewed at wileyonlinelibrary.com]

In analogy to Figure 8, Figure 9 shows the decomposition of the change in terms of the water vapor mixing ratio change within H_a. Though we did not consider changes in the water vapor mixing ratio in the analyses discussed earlier herein, Figure 9 gives evidence that for all simulated cases there is a positive feedback; that is, the CSs display a higher water vapor mixing ratio than the NFs do. The evolution, however, is controlled by different processes partly counteracting each other, as presented in Equation (2). Deposition of fog droplets is the dominating process and makes up most of the net increase in water vapor mixing ratio of the difference between CS and NF (with values up to 0.23 g·kg^{-1}; Figure 9). Naturally, deposition of droplets is only present in the NF cases. The significance of this contribution is linked again to the strength of the fog and increases with increasing LWP and fog duration. It has been known that this process is strong in deep radiation fogs as the deposition rate is typically in the range of 20 g·m^{-2} · hr^{-1} (e.g., Boutle *et al.*, 2018), meaning the liquid water content within the fog layer is replenished every 0.5–2.0 hr, which is also seen in the present dataset (26 g·m^{-2} · hr^{-1} for the baseline simulation during the mature phase of the fog). The second largest contribution to the differences is caused by the LHF due to evapotranspiration of vegetation (LHF$_{veg}$). These differences in LHF$_{veg}$ are driven in particular by the fact that the higher temperatures in CSs result in a higher saturation vapor pressure deficit, which causes higher evapotranspiration. As in both CS and NF almost all the dew produced during the night (which is in total more for the CSs due to a colder surface) is evaporated at $t_{a,q}$, the net contribution is nearly zero (yellow markers, LHF$_{liq}$). For all cases, a residual close to zero observed.

As discussed earlier, we see a net gain in the water vapor mixing ratio when comparing the CS against NF cases. One thus might expect that the RH in the daytime becomes higher, but we observe the opposite (Figure 10) for almost all cases. This can be explained by the fact that we also find significantly higher BL temperatures (contribution of higher temperature to RH decrease is illustrated by the arrows in Figure 10) for the CSs compared with the NFs, so that the air can hold significantly more water vapor than gain due to non-existing fog development during nighttime. As a direct consequence, we can conclude that the misrepresentation of nocturnal radiation fog can lead to a too low RH during daytime. Therefore, failing to resolve fog fortunately does not favor an artificial cloud development during daytime. However, in some situations, when RH near the top of the CBL is close to 100% (assuming the NF as the reference), such errors in the RH might suppress the development of, for example, shallow cumulus clouds, which would develop if the fog were captured during nighttime.

4 | SUMMARY AND CONCLUSION

Nocturnal radiation fog is frequently misrepresented in numerical models. The potential effect of failing to simulate a nocturnal deep radiation fog on the development of the daytime BL was studied in this article. High-resolution LESs were employed for this purpose. A set of typical

conditions prone to fog formation in spring and autumn seasons for the midlatitudes was simulated. By comparing pairs of simulations where deep fog was allowed to develop in one case of each pair and fog formation was suppressed in the other, the potential effects on the daytime CBL were analyzed. Here, cases in which fog did not dissipate completely and remained as low-level stratus during daytime were excluded.

The temperature within the CBL was found to be up to 2.5 K warmer for the CSs than in the NFs after fog dissipation, which was accompanied by a deeper CBL by up to 200 m. However, these differences decreased over time (due to approximately 25% larger Bowen ratios in the NFs) and were most extreme shortly after the dissipation of fog. Furthermore, water vapor mixing ratios were observed to be up to 10% lower in the NFs, whereas temperatures were significantly warmer. As the latter was the dominant effect, a generally lower RH at the top of the BL was produced in the CSs. As a direct consequence, the development of clouds during daytime (e.g., shallow cumulus clouds) might be suppressed by the misrepresentation of nocturnal fog. The differences between CSs and NFs during the day were exacerbated by fog thickness and duration. The thickness of the fog is neither an explicit parameter to be varied (or known a priori) nor an environmental condition, but rather an implicit result of the meteorological circumstances. Hence, a rather complex pattern emerges with respect whether other parameters (e.g., wind) influence the development of fog on CBL. Nevertheless, it can be concluded that the deviation in daytime CBL properties between CSs and NFs are amplified by circumstances that favor more extreme fog events (e.g., less incoming solar radiation during the day). Long-wave atmospheric cooling (in terms of temperature deviation) and droplet deposition (in terms of mixing ratio) were identified as the most important processes that can trigger differences between CSs and NFs. Therefore, special attention should be given to the representation of those processes in numerical models.

The error that is induced by failing to resolve a deep radiation fog event in the NBL (under spring and autumn conditions) can be significant for daytime CBL development. Thus, these findings are not following a potential straight conclusion based on the studies of van Stratum and Stevens (2015; 2018), who showed that misrepresentation of the NBL due to an underresolved NBL has no relevant implications for daytime convection (under summer conditions). Nevertheless, in agreement with van Stratum and Stevens (2015), artificial moist daytime convection is usually not initiated by non-resolved fog in the present study. However, how strong the error is in simulating the transition from deep fog to low-level stratus can only be conjectured, as such cases were excluded in this study. To extend this work to account for such cases would be the starting point for a follow-up study.

Though perhaps impaired by limited horizontal extent (i.e., neglecting advection effects and non-local contributions) and idealized assumptions (i.e., fog misrepresentation is achieved by turning off cloud microphysics), the potential of nocturnal fog to effect CBL development is shown and quantified by the results presented here. It is likely that the feedback on the daytime BL that was identified in this idealized setting will also be present in operational models (e.g., NWP models). To asses this statement, a rigorous comparison of deep fog events that were not captured (or not captured adequately) by NWP models should be performed and respective daytime forecasts should be compared with in-situ observations of such situations.

ACKNOWLEDGEMENTS

All simulations were carried out on the computer clusters of the North-German Supercomputing Alliance (HLRN). Python 3.8 was used for data analysis and visualization. The PALM code can be accessed at https://gitlab.palm-model.org/. We sincerely thank Marie Mazoyer and Christine Lac for reviewing this article. Their numerous valuable comments helped to improve the manuscript. Open Access funding enabled and organized by Projekt DEAL. [Correction added on 28 September 2022, after first online publication: The Acknowledgements section has been amended in this updated version of the article.]

CONFLICT OF INTEREST

The authors declare no conflict of interest. The funders had no role in the design of the study, in the collection, analyses, or interpretation of data, in the writing of the manuscript, or in the decision to publish the results.

DATA AVAILABILITY STATEMENT

Model steering data and output files of the simulations presented are supplied at https://doi.org/10.25835/0019390.

ORCID

Johannes Schwenkel https://orcid.org/0000-0002-3985-4498

REFERENCES

Ackerman, A.S., vanZanten, M.C., Stevens, B., Savic-Jovcic, V., Bretherton, C.S., Chlond, A., Golaz, J.-C., Jiang, H., Khairoutdinov, M., Krueger, S.K., Lewellen, D.C., Lock, A., Moeng, C.-H., Nakamura, K., Petters, M.D., Snider, J.R., Weinbrecht, S. and Zulauf, M. (2009) Large-eddy simulations of a drizzling, stratocumulus-topped marine boundary layer. *Monthly Weather Review*, 137(3), 1083–1110.

Beare, R.J., Macvean, M.K., Holtslag, A.A., Cuxart, J., Esau, I., Golaz, J.-C., Jimenez, M.A., Khairoutdinov, M., Kosovic, B.,

Lewellen, D., Lund, T.S., Lundquist, J.K., Mccabe, A., Moene, A.F., Noh, Y., Raasch, S. and Sullivan, P. (2006) An intercomparison of large-eddy simulations of the stable boundary layer. *Boundary-Layer Meteorology*, 118(2), 247–272.

Bergot, T. (2013) Small-scale structure of radiation fog: A large-eddy simulation study. *Quarterly Journal of the Royal Meteorological Society*, 139(673), 1099–1112.

Bergot, T. and Guedalia, D. (1994) Numerical forecasting of radiation fog. Part I: Numerical model and sensitivity tests. *Monthly Weather Review*, 122(6), 1218–1230.

Boutle, I., Angevine, W., Bao, J.-W., Bergot, T., Bhattacharya, R., Bott, A., Ducongé, L., Forbes, R., Goecke, T., Grell, E., Hill, A., Igel, A.L., Kudzotsa, I., Lac, C., Maronga, B., Romakkaniemi, S., Schmidli, J., Schwenkel, J., Steeneveld, G.-J. and Vié, B. (2022) Demistify: A large-eddy simulation (LES) and single-column model (SCM) intercomparison of radiation fog. *Atmospheric Chemistry and Physics*, 22(1), 319–333. https://doi.org/10.5194/acp-22-319-2022.

Boutle, I., Price, J., Kudzotsa, I., Kokkola, H. and Romakkaniemi, S. (2018) Aerosol–fog interaction and the transition to well-mixed radiation fog. *Atmospheric Chemistry and Physics*, 18(11), 7827–7840.

Brown, A., Cederwall, R., Chlond, A., Duynkerke, P., Golaz, J.C., Khairoutdinov, M., Lewellen, D.C., Lock, A.P., MacVean, M.K., Moeng, C.-H., Neggers, R.A.J., Siebesma, A.P. and Stevens, B. (2002) Large-eddy simulation of the diurnal cycle of shallow cumulus convection over land. *Quarterly Journal of the Royal Meteorological Society*, 128(582), 1075–1093.

Clough, S.A., Shephard, M.W., Mlawer, E.J., Delamere, J.S., Iacono, M.J., Cady-Pereira, K., Boukabara, S. and Brown, P.D. (2005) Atmospheric radiative transfer modeling: a summary of the AER codes. *Journal of Quantitative Spectroscopy & Radiative Transfer*, 91(2), 233–244.

Couvreux, F., Bazile, E., Rodier, Q., Maronga, B., Matheou, G., Chinita, M.J., Edwards, J., van Stratum, B.J.H., van Heerwaarden, C.C., Huang, J., Moene, A.F., Cheng, A., Fuka, V., Basu, S., Bou-Zeid, E., Canut, G. and Vignon, E. (2020) Intercomparison of large-eddy simulations of the Antarctic boundary layer for very stable stratification. *Boundary-Layer Meteorology*, 176(3), 369–400.

Deardorff, J.W. (1980) Stratocumulus-capped mixed layers derived from a three-dimensional model. *Boundary-Layer Meteorology*, 18(4), 495–527.

Fernando, H. and Weil, J. (2010) Whither the stable boundary layer? A shift in the research agenda. *Bulletin of the American Meteorological Society*, 91(11), 1475–1484.

Gehrke, K.F., Sühring, M. and Maronga, B. (2021) Modeling of land-surface interactions in the PALM model system 6.0: Land surface model description, first evaluation, and sensitivity to model parameters. *Geoscientific Model Development*, 14(8), 5307–5329.

Haeffelin, M., Bergot, T., Elias, T., Tardif, R., Carrer, D., Chazette, P., Colomb, M., Drobinski, P., Dupont, E., Dupont, J.-C., Gomes, L., Musson-Genon, L., Pietras, C., Plana-Fattori, A., Protat, A., Rangognio, J., Raut, J.-C., RÃĬmy, S., Richard, D., Sciare, J. and Zhang, X. (2010) PARISFOG: Shedding new light on fog physical processes. *Bulletin of the American Meteorological Society*, 91(6), 767–783.

Izett, J.G., van de Wiel, B.J., Baas, P., van Hooft, J.A. and Schulte, R.B. (2019) Dutch fog: On the observed spatio-temporal variability of fog in the Netherlands. *Quarterly Journal of the Royal Meteorological Society*, 145(723), 2817–2834.

Maronga, B., Banzhaf, S., Burmeister, C., Esch, T., Forkel, R., Fröhlich, D., Fuka, V., Gehrke, K.F., Geletič, J., Giersch, S., Gronemeier, T., Groß, G., Heldens, W., Hellsten, A., Hoffmann, F., Inagaki, A., Kadasch, E., Kanani-Sühring, F., Ketelsen, K., Khan, B.A., Knigge, C., Knoop, H., Krč, P., Kurppa, M., Maamari, H., Matzarakis, A., Mauder, M., Pallasch, M., Pavlik, D., Pfafferott, J., Resler, J., Rissmann, S., Russo, E., Salim, M., Schrempf, M., Schwenkel, J., Seckmeyer, G., Schubert, S., Sühring, M., von Tils, R., Vollmer, L., Ward, S., Witha, B., Wurps, H., Zeidler, J. and Raasch, S. (2020a) Overview of the PALM model system 6.0. *Geoscientific Model Development*, 13(3), 1335–1372.

Maronga, B. and Bosveld, F. (2017) Key parameters for the life cycle of nocturnal radiation fog: A comprehensive large-eddy simulation study. *Quarterly Journal of the Royal Meteorological Society*, 143(707), 2463–2480.

Maronga, B., Knigge, C. and Raasch, S. (2020b) An improved surface boundary condition for large-eddy simulations based on Monin–Obukhov similarity theory: Evaluation and consequences for grid convergence in neutral and stable conditions. *Boundary-Layer Meteorology*, 174(2), 297–325.

Maronga, B. and Li, D. (2022) An investigation of the grid sensitivity in large-eddy simulations of the stable boundary layer. *Boundary-Layer Meteorology*, 182(2), 251–273.

Mazoyer, M., Lac, C., Thouron, O., Bergot, T., Masson, V. and Musson-Genon, L. (2017) Large eddy simulation of radiation fog: Impact of dynamics on the fog life cycle. *Atmospheric Chemistry and Physics*, 17(21), 13017–13035.

Mellado, J.P. (2017) Cloud-top entrainment in stratocumulus clouds. *Annual Review of Fluid Mechanics*, 49, 145–169.

Morrison, H., Curry, J.A. and Khvorostyanov, V. (2005) A new double-moment microphysics parameterization for application in cloud and climate models. Part I: Description. *Journal of the Atmospheric Sciences*, 62(6), 1665–1677.

Nakanishi, M. (2000) Large-eddy simulation of radiation fog. *Boundary-Layer Meteorology*, 94(3), 461–493.

Rémy, S. and Bergot, T. (2009) Assessing the impact of observations on a local numerical fog prediction system. *Quarterly Journal of the Royal Meteorological Society*, 135(642), 1248–1265.

Schwenkel, J. and Maronga, B. (2019) Large-eddy simulation of radiation fog with comprehensive two-moment bulk microphysics: Impact of different aerosol activation and condensation parameterizations. *Atmospheric Chemistry and Physics*, 19(10), 7165–7181. https://doi.org/10.5194/acp-19-7165-2019.

Schwenkel, J. and Maronga, B. (2020) Towards a better representation of fog microphysics in large-eddy simulations based on an embedded Lagrangian cloud model. *Atmosphere*, 11(5), 466.

Seifert, A. and Beheng, K.D. (2001) A double-moment parameterization for simulating autoconversion, accretion and selfcollection. *Atmospheric Research*, 59–60, 265–281.

Seifert, A. and Beheng, K.D. (2006) A two-moment cloud microphysics parameterization for mixed-phase clouds. Part 1: Model description. *Meteorology and Atmospheric Physics*, 92(1), 45–66. https://doi.org/10.1007/s00703-005-0112-4.

Smith, D., Renfrew, I., Price, J. and Dorling, S. (2018) Numerical modelling of the evolution of the boundary layer during a radiation fog event. *Weather*, 73(10), 310–316.

Steeneveld, G.J. and de Bode, M. (2018) Unravelling the relative roles of physical processes in modelling the life cycle of a warm

radiation fog. *Quarterly Journal of the Royal Meteorological Society*, 144(714), 1539–1554.
Steeneveld, G., Ronda, R. and Holtslag, A. (2015) The challenge of forecasting the onset and development of radiation fog using mesoscale atmospheric models. *Boundary-Layer Meteorology*, 154(2), 265–289.
van Stratum, B.J. and Stevens, B. (2015) The influence of misrepresenting the nocturnal boundary layer on idealized daytime convection in large-eddy simulation. *Journal of Advances in Modeling Earth Systems*, 7(2), 423–436.
van Stratum, B.J. and Stevens, B. (2018) The impact of vertical mixing biases in large-eddy simulation on nocturnal low clouds. *Journal of Advances in Modeling Earth Systems*, 10(6), 1290–1303.
Toledo, F., Haeffelin, M., Wærsted, E. and Dupont, J.C. (2021) A new conceptual model for adiabatic fog. *Atmospheric Chemistry and Physics*, 21(17), 13099–13117.
Vilà-Guerau de Arellano, J. (2007) Role of nocturnal turbulence and advection in the formation of shallow cumulus over land. *Quarterly Journal of the Royal Meteorological Society*, 133(628), 1615–1627.
Wainwright, C. and Richter, D. (2021) Investigating the sensitivity of marine fog to physical and microphysical processes using large-eddy simulation. *Boundary-Layer Meteorology*, 181(2), 473–498.
Wærsted, E.G., Haeffelin, M., Steeneveld, G.J. and Dupont, J.C. (2019) Understanding the dissipation of continental fog by analysing the LWP budget using idealized LES and in situ observations. *Quarterly Journal of the Royal Meteorological Society*, 145(719), 784–804.
Wicker, L.J. and Skamarock, W.C. (2002) Time-splitting methods for elastic models using forward time schemes. *Monthly Weather Review*, 130(8), 2088–2097.
Williamson, J. (1980) Low-storage Runge–Kutta schemes. *Journal of Computational Physics*, 35(1), 48–56.

SUPPORTING INFORMATION

Additional supporting information can be found online in the Supporting Information section at the end of this article.

How to cite this article: Schwenkel, J. & Maronga, B. (2022) On the effect of nocturnal radiation fog on the development of the daytime convective boundary layer: A large-eddy simulation study. *Quarterly Journal of the Royal Meteorological Society*, 148(748), 3166–3183. Available from: https://doi.org/10.1002/qj.4352

APPENDIX A. PROCESS CONTRIBUTIONS TERMS

This appendix explains how we derive contributions for single processes of Equations 1 and 2 from the model output. SHF, LHF, LWP, and F_{dep} are given as horizontal averaged time series, which are provided every $\Delta t_{\mathrm{ts}} = 10\,\mathrm{s}$. The short-wave heating rates due to absorption and the atmospheric long-wave cooling rates are provided as horizontally averaged and temporal mean profiles as model output every 5 min.

A.1 Temperature

Following the approach presented in Section 2.3, the process contribution for the SHF is approximated by

$$\left\langle \frac{\delta\theta_{\mathrm{SHF}}}{dt} \right\rangle = \frac{1}{\rho c_p} \frac{\mathrm{SHF_{CS}} - \mathrm{SHF_{NF}}}{H_{\mathrm{a}}}, \tag{A1}$$

where SHF has units of $\mathrm{W{\cdot}m^{-2}}$, ρ is the air density (approximated by $1.29\,\mathrm{kg{\cdot}m^{-3}}$), and $c_p = 1{,}005\,\mathrm{J{\cdot}kg^{-1}\cdot K^{-1}}$ the specific heat capacity of air. Moreover, it is assumed that $T \approx \theta$, which is justified for not too large values of H_{a}. Contributions for radiative heating rates are calculated as

$$\left\langle \frac{\delta\theta_{\mathrm{lw}}}{dt} \right\rangle = \frac{\langle (R_{\mathrm{lw}})_{\mathrm{CS}} - (R_{\mathrm{lw}})_{\mathrm{NF}} \rangle}{H_{\mathrm{a}}}, \tag{A2}$$

$$\left\langle \frac{\delta\theta_{\mathrm{sw}}}{dt} \right\rangle = \frac{\langle (R_{\mathrm{sw}})_{\mathrm{CS}} - (R_{\mathrm{sw}})_{\mathrm{NF}} \rangle}{H_{\mathrm{a}}}, \tag{A3}$$

with R_{lw} and R_{sw} as the long- and short-wave heating rates ($\mathrm{K{\cdot}hr^{-1}}$), respectively, which are directly calculated within the coupled RRTMG (Clough *et al.*, 2005). Moreover, the temperature is increased (decreased) by the release of latent heat from condensation (evaporation). However, phase transitions within the atmosphere are only simulated in the NFs. Subsequently, we can substitute the microphysics contribution to

$$\left\langle \frac{\delta\theta_{\mathrm{micro}}}{dt} \right\rangle = \frac{1}{\rho c_p} \frac{-l_{\mathrm{v}} \left(\frac{\mathrm{LWP}(t)_{\mathrm{NF}} - \mathrm{LWP}(t-1)_{\mathrm{NF}}}{\Delta t_{\mathrm{ts}}} + F_{\mathrm{dep,NF}} \right)}{H_{\mathrm{a}}}, \tag{A4}$$

where $l_{\mathrm{v}} = 2.5 \times 10^6\,\mathrm{J{\cdot}kg^{-1}}$ is the specific latent heat of vaporization, LWP is the liquid water path, and F_{dep} is the surface droplet deposition flux ($\mathrm{kg{\cdot}m^{-2}\cdot m{\cdot}s^{-1}}$). Condensation and evaporation rates are implicitly calculated by the change in LWP and the loss due to deposition. For assessing which process is mostly responsible for temperature differences, Equations A1–A4 are integrated to the point in time where differences in temperature were the largest ($t_{\mathrm{a},\theta}$). Exemplary Equation (A1) can be written as

$$\langle \delta\theta_{\mathrm{SHF}} \rangle = \int_0^{t_{\mathrm{a},\theta}} \frac{1}{\rho c_p} \frac{\mathrm{SHF_{CS}} - \mathrm{SHF_{NF}}}{H_{\mathrm{a}}} dt, \tag{A5}$$

and Equations A2–A4 are integrated analogously. The time-integrated deviation between the modeled and calculated differences (of the resolved process analysis) is termed the residual and calculated as

$$\langle \delta\theta_{\mathrm{Res}} \rangle = \langle \delta\theta_{t_{a,\theta}} \rangle - \langle \delta\theta_{\mathrm{LHF,veg}} \rangle - \langle \delta\theta_{\mathrm{LHF,liq}} \rangle - \langle \delta\theta_{\mathrm{dep}} \rangle. \tag{A6}$$

A.2 Water vapor mixing ratio

As for the water vapor mixing ratio, the process contributions are only shown as time-integrated analysis equations and also presented in the integrated form. The difference of the gain (loss) due to a positive (negative) $\mathrm{LHF_{veg}}$ between CS and NF is given by

$$\langle \delta q_{\mathrm{LHF,veg}} \rangle = \int_0^{t_{a,q}} \frac{1}{\rho\, l_v} \frac{\mathrm{LHF_{veg,CS}} - \mathrm{LHF_{veg,NF}}}{H_a} dt, \tag{A7}$$

where $\mathrm{LHF_{veg}}$ has units of $\mathrm{W{\cdot}m^{-2}}$. Analogously, for $\mathrm{LHF_{liq}}$ we have

$$\langle \delta q_{\mathrm{LHF,liq}} \rangle = \int_0^{t_{a,q}} \frac{1}{\rho\, l_v} \frac{\mathrm{LHF_{liq,CS}} - \mathrm{LHF_{liq,NF}}}{H_a} dt. \tag{A8}$$

For the time-integrated analysis of the contribution by microphysics, F_{micro} can be substituted with the deposition rate F_{dep}. The underlying assumption is that (integrated over the life cycle of the fog) condensation and evaporation is net zero. Hence, the only sink for the water vapor mixing ratio is the deposited amount of liquid water to the surface. Since only the NF case suffers a loss of humidity to due deposition of fog droplets, this is considered by

$$\langle \delta q_{\mathrm{dep}} \rangle = \int_0^{t_{a,q}} \frac{F_{\mathrm{dep}}}{H_a} dt. \tag{A9}$$

The residual is analogous to Equation (A6), calculated by

$$\langle \delta q_{\mathrm{Res}} \rangle = \langle \delta q_{t_{a,q}} \rangle - \langle \delta q_{\mathrm{LHF,veg}} \rangle - \langle \delta q_{\mathrm{LHF,liq}} \rangle - \langle \delta q_{\mathrm{dep}} \rangle. \tag{A10}$$